Protection of zirconium by alumina- and chromia-forming iron alloys under high-temperature steam exposure ☆

Kurt A. Terrani [a,*], Chad M. Parish [b], Dongwon Shin [b], Bruce A. Pint [b]

[a] *Fuel Cycle and Isotopes Division, Oak Ridge National Laboratory, Oak Ridge, TN 37831, USA*
[b] *Materials Science and Technology Division, Oak Ridge National Laboratory, Oak Ridge, TN 37831, USA*

ARTICLE INFO

ABSTRACT

The viability of advanced oxidation-resistant Fe-base alloys to protect zirconium from rapid oxidation in high-temperature steam environments has been examined. Specimens were produced such that outer layers of FeCrAl ferritic alloy and Type 310 austenitic stainless steel were incorporated on the surface of zirconium metal slugs. The specimens were exposed to high-temperature 0.34 MPa steam at 1200 and 1300 °C. The primary degradation mechanism for the protective layer was interdiffusion with the zirconium, as opposed to high-temperature oxidation in steam. The FeCrAl layer experienced less degradation and protected the zirconium at 1300 °C for 8 h. Constituents of the Fe-base alloys rapidly diffused into the zirconium and resulted in the formation of various intermetallic layers at the interface and precipitates inside the bulk zirconium. The nature of this interaction for FeCrAl and 310SS has been characterized by use of microscopic techniques as well as computational thermodynamics. Finally, a reactor physics discussion on the applicability of these protective layers in light-water-reactor nuclear fuel structures is offered.

Published by Elsevier B.V.

1. Introduction

Zirconium alloys are currently the sole choice of cladding material for nuclear fuel elements across the world's fleet of commercial light water reactors (LWRs). Zirconium's small neutron capture cross section ($\sim$7% that of iron) yields an ideal thermal utilization factor for sustained criticality in nuclear reactor cores. Six decades of active alloy development have produced tailored alloy chemistries and processing methodologies that provide adequate corrosion behavior under pressurized or boiling water reactor conditions while limiting irradiation growth and creep [1]. All of the above highlight the attractive properties of zirconium alloys for nuclear fuel cladding and structural components in conventional oxide fuel bundles in LWRs. These same attributes are the basis for utilizing zirconium alloys as the matrix of choice for the recently proposed metal matrix microencapsulated (M3) fuels [2,3].

Reactor accident scenarios challenge the integrity of zirconium alloy fuel cladding tubes. A variety of accident sequences could result in loss of core cooling capability inside the core and a loss of coolant that would eventually drive up the fuel temperature and expose the cladding to a high-temperature steam environment. Examples of such accident scenarios are a design-basis loss-of-coolant accident (LOCA) or a beyond-design-basis station blackout (SBO) accident. Oxidation kinetics of zirconium alloys in high-temperature steam environments have been studied extensively [4–7]. At temperatures above 1050 °C (but below 1525 °C, which marks the tetragonal-to-cubic zirconia transition temperature [8]), the oxide remains adherent and parabolic oxidation kinetics, although rapid in magnitude, are observed up to long periods. The zirconium oxidation reaction in steam is associated with a large enthalpy of formation (-586 kJ/mol Zr [4]) and accompanied by hydrogen gas production. The rate of heat production due to oxidation of the Zr alloy cladding becomes significant enough at temperatures above 1200 °C to potentially surpass decay heat production in the fuel and become the dominant source of temperature rise in the fuel. This self-catalytic reaction quickly drives up the temperature in the fuel and results in complete oxidation of the entire cladding.

The work presented here examines the viability of oxidation-resistant Fe-based alloys for protecting zirconium alloys from rapid oxidation in a high-temperature steam environment. This study was specifically undertaken to examine the applicability of this approach for protection of M3 fuels [3] under high-temperature steam environments. The M3 concept involves an integral rod for which the cladding has been eliminated. Inside the fuel rod,

microencapsulated fuel particles (i.e., BIstructural or TRIstructural ISOtropic or in short BISO or TRISO) are dispersed in a zirconium alloy matrix. However, the results presented here are also applicable to composite cladding tube structures, where a thin Fe-base alloy layer would cover the zirconium alloy cladding. The protective oxide layers formed by the Fe-based alloy outer layer are intended to eliminate rapid heat and hydrogen generation that results from oxidation of zirconium metal and provide larger margins of safety during accident scenarios up to long periods and temperatures beyond 1200 °C (but less than ~1400–1500 °C, which marks the melting point of most iron alloys). In this study, a ferritic FeCrAl alloy and an austenitic Type 310 stainless steel alloy that are alumina- and chromia-forming, respectively, were investigated. The two alloys were chosen on the basis of results from a recent study at ORNL that identified excellent performance of these alloys at 1200 °C high-pressure steam environments [9–11].

2. Experimental approach

To simplify the experiment, zirconium was encapsulated in cans of the two iron alloys and exposed to a high-temperature high-pressure steam environment. Test specimens were fabricated by hot isostatic pressing (HIP) of zirconium metal powder inside these cans, a methodology consistent with the proposed fabrication route for M3 fuels [3]. Table 1 describes the detailed composition of the zirconium as well as the laboratory cast FeCrAl alloy and commercial 310SS used during fabrication. By using the HIP process, formation of a dense zirconium core fully bonded to the protective layer was achieved. Fig. 1 shows the configuration of the cans that were initially filled with zirconium metal powder. The cans were subsequently sealed by electron-beam welding under a vacuum environment. The specimens were then HIPed (AIP Inc., Columbus, OH) at 900 °C for 1 h under an argon gas pressure of 30 MPa. The HIP temperature of 900 °C was chosen to be well below the lowest eutectic point in the Zr–Fe binary phase diagram. Fig. 2 shows the binary phase diagrams of zirconium with iron, chromium, nickel, and aluminum over the temperature range 700–1500 °C [12–14]. Note that by examining the ternary phase diagrams for the iron–chromium–zirconium system [15], one can readily note that the presence of chromium shifts the temperatures of the liquid phase even higher.

Four zirconium-bearing cans from each alloy were fabricated using the HIP methodology described. Metallographic mounts were prepared from the cross section of one capsule from each alloy after HIP fabrication to evaluate the Zr alloy interface after fabrication at 900 °C. Fig. 3 shows the interface between the Zr alloy and the 310SS and FeCrAl alloy layers in the as-fabricated (HIPed) state. In the case of FeCrAl alloy, only a thin interaction layer at the interface is present. For 310SS, a slightly thicker uniform layer at the interface is present while precipitates are observed inside the Zr alloy up to 30–40 μm away from the interface. Interaction of Zr and Zircaloy with pure iron and austenitic steels in the temperature range of interest has been examined previously, where it has been shown that the nature and extent of interaction is very sensitive to the alloying elements in the zirconium and iron [16–18]. Consistent with the current observation, much more extensive interaction between zirconium and austenitic-type steels that contain nickel has been reported.
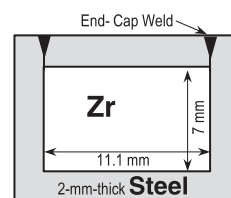

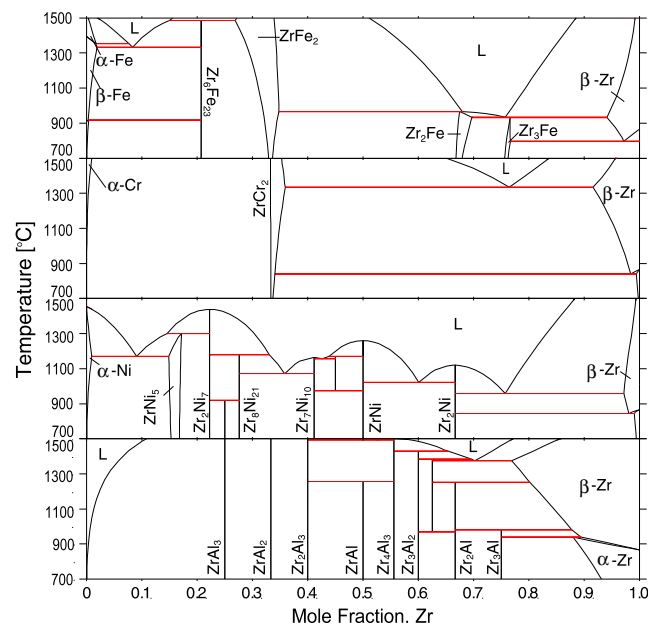Fig. 1. Cross section of zirconium slugs encapsulated in oxidation-resistant iron alloy layers.

Fig. 2. Binary Zr–Fe, Zr–Cr, Zr–Ni, and Zr–Al phase diagrams from 700 to 1500 °C [12–14].

The remaining HIPed cans, three from each alloy, were exposed to the high-temperature high-pressure steam environments. Detailed description of the high-temperature and pressure steam test apparatus is provided elsewhere [19]. Briefly, the system consists of a SiC pressure vessel (~1 m in length with a 4 cm inner diameter) that is heated with a resistance furnace from the outside. Inside the pressure vessel, an alumina rod is used to hang samples vertically. The gas enters bottom of the vessel and flows upward to exit the outlet at the top. The three steam exposures are described in Table 2. The environment during the furnace ramp was kept under argon, and upon reaching the isothermal test temperature, it was switched to pure steam.

The capsules exposed to high-temperature steam environments were also cross-sectioned and prepared for microscopic examination. All the cross sections were examined with a JEOL 6500 field-emission gun, scanning electron microscope (FEG-SEM) operating at 10 kV accelerating potential. Additionally, a detailed analysis, consisting of coupled electron backscatter diffraction (EBSD) and energy-dispersive X-ray spectroscopy (EDS) [20,21], was performed to examine the interfaces between zirconium metal and the iron alloy layers for the samples exposed to high-temperature

Table 1
Composition of zirconium metal powder as well as 310SS and FeCrAl alloys in percent mass determined by inductively coupled plasma and combustion techniques.

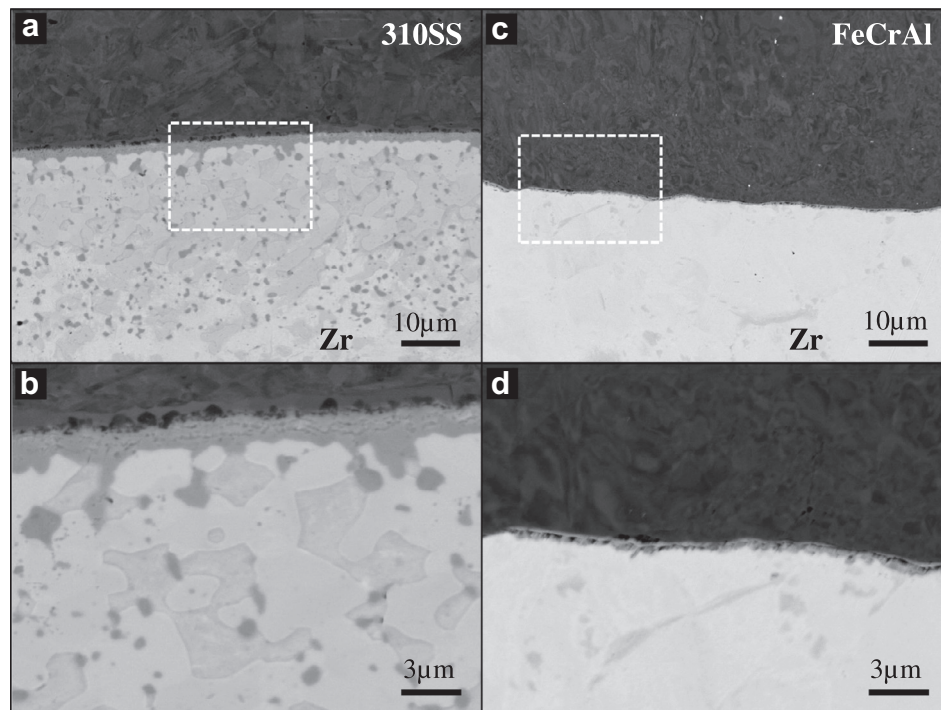| Alloy	Al	C	Co	Cr	Cu	Fe	Hf	Mn	Mo	N	Ni	O	Si	Y	Zr
310SS		0.044	0.15	25.38	0.11	51.85		1.89	0.13	0.058	19.52	0.006	0.7		
FeCrAl	5.18	0.002	<0.01	20.25	<0.01	74.4	<0.01	<0.01	<0.01	0.0005	<0.01	0.003	<0.01	<0.01	0.15
Zr	0.005	0.036		0.069		0.3	1.04			0.01	0.022	0.24	<0.005	<0.001	98.2

Fig. 3. SEM backscattered electron images of the interface between zirconium and (a and b) 310SS and (c and d) FeCrAl alloy after HIPing at 900 °C for 1 h.

Table 2
High-temperature steam exposure test conditions.

Test ID	Temperature (°C)	Time (h)	Pressure (MPa)	Gas velocity (cm/s)
1	1200	18	0.34	1.67
2	1200	48	0.34	1.67
3	1300	8	0.34	1.75

steam environments. The full details of this analysis will be published in the upcoming microscopy literature.

Finally a computational thermodynamic modeling approach, CALPHAD (CALculation of PHAse Diagram) [22], was employed to compliment the experimental observations. Thermodynamic descriptions for the individual phases in the constituent binary, ternary, and quaternaries of both 310SS (Fe–Cr–Ni–Mn) and FeCrAl (Fe–Cr–Al) were obtained from the TCFE6 iron/steel database as implemented in Thermo-Calc™ version S [23]. Gibbs free energy functions for the binaries with zirconium were obtained from the literature (Fe–Zr [12], Cr–Zr [13], Ni–Zr [14], Mn–Zr [13], and Al–Zr [13]) and combined with the TCFE6 database.

3. Results and analysis

3.1. Macroscopic examination

Fig. 4 shows the iron-alloy-encapsulated zirconium slugs after fabrication and exposure to the high-temperature steam environments. The as-fabricated images show the welded cap on top of the cans and more HIPing deformation was noted for the FeCrAl can suggesting more densification. Cross sections of the HIPed specimens revealed full Zr densification in the FeCrAl can where no porosity was observed. In case of the 310SS can some porosity was observed in the core Zr region. This is attributed to the higher strength of 310SS at 900 °C as compared to FeCrAl [24,25]. However, as shown in Fig. 3, a full metallurgical bond suitable for this experiment was present at the interface between the 310SS and Zr.

The 1200 °C steam exposures showed that effective protection of zirconium by the 2-mm-thick oxidation-resistant layers could be achieved for up to 48 h. However, the 1300 °C exposure revealed a drastic contrast between the protectiveness of the two different alloys. The FeCrAl can remained protective for the 8 h exposure, while the 310SS can failed allowing the Zr metal inside to oxidize. The oxidation reaction was accompanied by a large volume expansion (the Pilling-Bedworth ratio [8] for zirconium oxide is ∼1.55).

3.2. Protective layer degradation mechanism

To separate the effects of can–Zr interaction and steam oxidation, separate disk coupons of FeCrAl and 310SS were exposed in the same steam experiments along with the cans. Fig. 5 shows the extent of oxidation of the two alloys after each test. Additionally, a calculated oxide layer thickness is also shown for Zircaloy-4 using the Pawel–Cathcart correlation [5]. The values for 310SS and FeCrAl were determined by examining the metallographic cross sections after each exposure. The extent of oxidation in the iron alloys examined here is well below that predicted for Zircaloy-4 and less than 1% of the thickness of the alloy layers in the cans. Therefore, the reason for the loss of protectiveness of 310SS at 1300 °C cannot be attributed to oxidation of the protective layer. Instead, interdiffusion is expected to lead to the formation of eutectic compositions suggested by the phase diagrams in Fig. 2. This is consistent with prior observations of detrimental interaction between 300-series austenitic stainless steel components and zirconium alloys in LWRs under simulated accident conditions [26,27].

3.3. Scanning electron microscopy

The samples exposed to steam were cross sectioned to characterize the starting condition and the interaction during the steam exposures. Fig. 6 shows the interaction between the FeCrAl can and the Zr alloy after the high-temperature exposures where
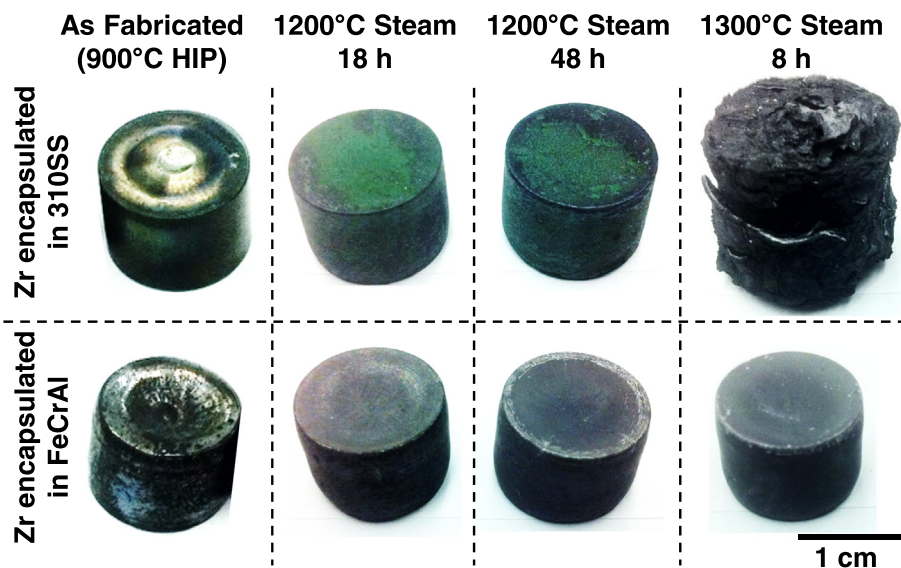
As Fabricated (900°C HIP) | **1200°C Steam 18 h** | **1200°C Steam 48 h** | **1300°C Steam 8 h**

Fig. 4. Iron-alloy-encapsulated zirconium slugs after HIP fabrication and exposure to high-temperature steam.
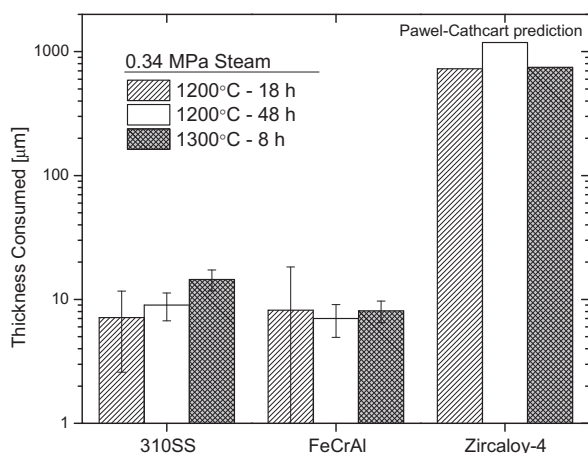

Fig. 5. Comparison of the extent of oxidation between 310SS, FeCrAl, and Zircaloy-4 (as predicted by Pawel–Cathcart correlation [5]) across the various test conditions. The bars show the average metal thickness consumed and the standard deviation of those measurements is noted.

extensive interdiffusion is apparent. For the specimen exposed for 18 h at 1200 °C, Fig. 7 shows EDS maps of the interaction layer. For all three cases, a uniform ~100 μm thick intermetallic layer at the interface is apparent. Using the coupled EDS/EBSD method, this layer was identified as $Zr(Cr,Fe)_2$ of space group $P6_3/mmc$ [28,29] instead of the cubic $ZrFe_2$ and $ZrCr_2$ phases (both with $Fd\bar{3}m$ space groups); the latter two are suggested to form at the test temperature by the binary phase diagrams in Fig. 2. Most of the Cr that diffused into the Zr alloy was trapped in this phase. Since Cr and Fe exhibit similar diffusivities in β-Zr (bcc) [30], the flux of these elements is expected to be proportional to their concentration in FeCrAl. Therefore, the larger flux of iron led to the formation of $ZrFe_2$ $Fd\bar{3}m$ space group) past the $Zr(Cr,Fe)_2$ layer. Upon cooling, zirconium likely underwent the β to α transformation and the solubility of iron in α-Zr (hcp) is negligible. As a result, $FeZr_2$ ($I4/mcm$ space group) formed in the Zr alloy where the iron concentration was sufficient. Zirconium also diffused into the ferritic alloy to form precipitates as shown in Fig. 6d. Contrary to the phase diagram in Fig. 2, these precipitates were identified as $ZrFe_2$. The Zr_6Fe_{23} phase is metastable and only forms in the presence of

oxygen [31]. EDS spectra show evidence of aluminum diffusion into the Zr alloy, where it appeared to be incorporated into the precipitates that form at the interface and within the bulk.

Fig. 8 summarizes the interactions observed for the 310SS cans after the steam exposures at 1200 °C. Fig. 9 provides EDS maps of the interaction layer between Zr and 310SS after 18 h at 1200 °C. In this case, two distinct uniform interaction layers, each roughly 200 μm thick, formed at the interface. The layer adjacent to the Zr alloy again consists of $Zr(Cr,Fe)_2$, while the layer adjacent to the 310SS formed due to Ni depletion from the steel. Rapid Ni transport into the Zr matrix occurred but did not form Ni-rich precipitates. Upon cooling, Ni was incorporated in the $(Fe,Ni)Zr_2$ precipitates (solid solution of $FeZr_2$ and $NiZr_2$ with a $I4/mcm$ space group) that form in the zirconium matrix. Ni depletion in the steel adjacent to the interface should result in the formation of ferrite. However, the layer is sigma phase ($P4_2/mnm$ space group), perhaps because the ferrite transformed during cool-down. The sigma phase also could be stabilized by Zr, but no sign of zirconium diffusion into the austenitic phase was apparent.

To summarize, both Fe-base alloys experienced significant interaction with the Zr alloy during the 1200 and 1300 °C exposures. Although not included in the above figures, constituents of the Fe-base alloys rapidly interdiffused, well into the center of the zirconium slug. The thickness of the interaction layer for the Zr–FeCrAl couple was roughly half that of Zr-310SS. In both cases, a complex series of brittle intermetallics form at the interface and within the bulk zirconium metal.

3.4. Computational thermodynamics

Fig. 10 shows the predicted phase fractions of individual intermetallics of 310SS-Zr and FeCrAl–Zr, which confirm most of the experimental observations at 800–1200 °C. The cubic $Zr(Fe,Cr)_2$ phase $Fd\bar{3}m$ space group) designated as the C15 laves phase structure dominates the phase stability of both 310SS and FeCrAl with zirconium. The present model does not accurately predict the phase stability of the hexagonal $Zr(Fe,Cr)_2$ phase in the $ZrFe_2$–$ZrCr_2$ pseudo-binary system. Fe–Zr does not have a phase conforming to the $P6_3/mmc$ space group in the stable phase diagram, but Cr–Zr has a small phase field with such a structure at high temperatures. However, Fe exhibits quite a large solubility in the Cr sublattice of the hexagonal $ZrCr_2$ phase, and the phase region of $Zr(Fe,Cr)_2$ is
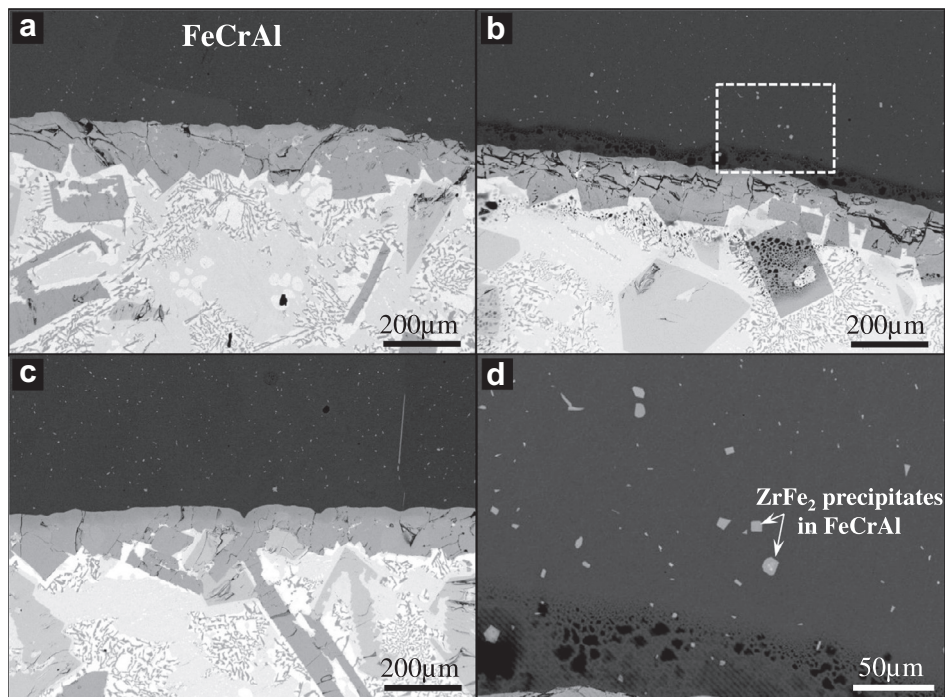
Fig. 6. Backscattered electron image of the interface between zirconium and FeCrAl after (a) 18 h at 1200 °C, (b) 48 h at 1200 °C, and (c) 8 h at 1300 °C and (d) Zr-containing precipitates forming inside the FeCrAl (48 h at 1200 °C) that attest to Zr diffusion into the alloy.
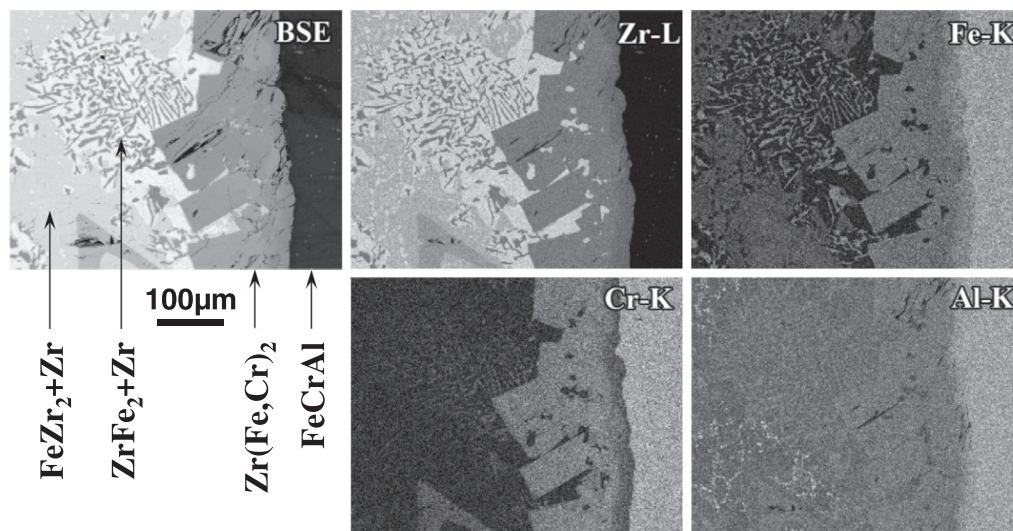

Fig. 7. EDS maps at Zr–FeCrAl interface after 18 h at 1200 °C.

fairly large in the $ZrFe_2$–$ZrCr_2$ pseudo-binary system. A complete thermodynamic description for $Zr(Fe,Cr)_2$ might be obtained from a comprehensive and self-consistent thermodynamic modeling of Cr–Fe–Zr; however, it is currently unavailable. Although a thermodynamic description for the hexagonal $Zr(Fe,Cr)_2$ phase is missing, predicted phase stabilities of 310SS-Zr and FeCrAl–Zr would be reliable with the current approach as they are mainly governed by binary intermetallics. The microscopic analysis elucidated the presence of the sigma phase in 310SS-Zr at 800 °C and it is confirmed in Fig. 10, while it does not appear in FeCrAl–Zr at the same temperature. At 1200 °C the phase fraction of liquid increases in both systems.

4. Discussion

4.1. Efficacy of oxidation-resistant protective layers

The protective iron alloy cans containing the Zr alloy slugs provided protection under high-temperature steam conditions compared to bare zirconium. This was achieved by limited oxygen inward diffusion in the slow-growing oxide which forms on the Fe-base alloys and acts as a solid state diffusion barrier. The alumina-forming FeCrAl alloy proved superior to the chromia-forming 310SS in that regard. Also, Fe-base alloys have a low oxygen solubility, further preventing any Zr alloy oxidation. By preventing the
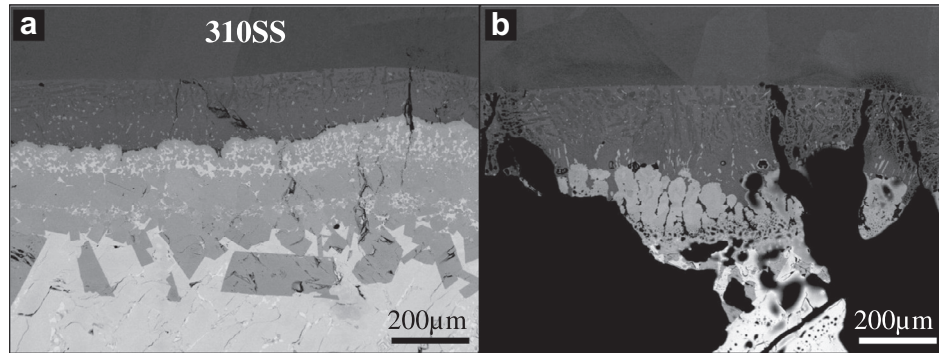
Fig. 8. Interface between zirconium and 310SS after (a) 18 h at 1200 °C and (b) 48 h at 1200 °C. No sign of Zr diffusion into the steel is apparent.
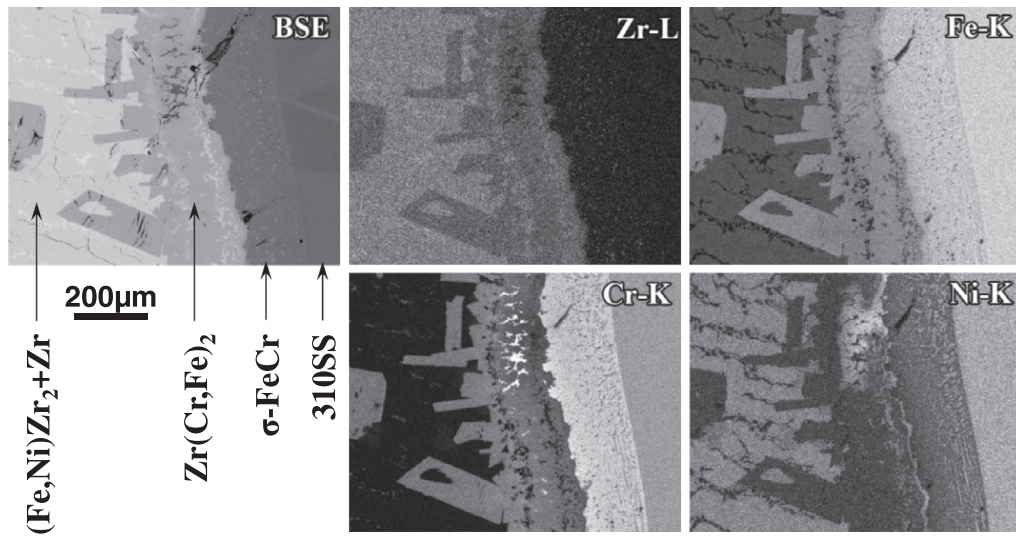

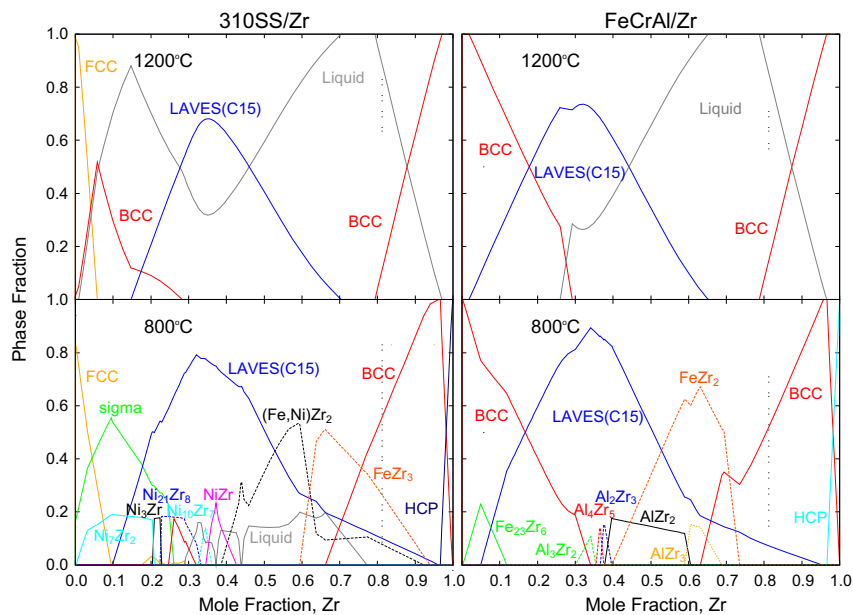**Fig. 9.** EDS maps at Zr-310SS interface after 18 h at 1200 °C.

Fig. 10. Predicted individual phase fractions of 310SS and FeCrAl in equilibrium with zirconium at 800 °C (bottom) and 1200 °C (top) from the computational thermodynamic approach.

oxidation of the Zr alloy, the associated enthalpy and hydrogen production also were prevented except for the 310SS can at 1300 °C. Consistent with prior observations [16–18], the main mechanism of degradation in these structures arose from the inter-diffusion between zirconium and iron alloys at high temperatures. It is expected that at temperatures close to the melting point of these alloys, the protectiveness of these layers will be compromised from the interaction with zirconium metal (as was shown for 310SS at 1300 °C after 8 h). However, depending on the specific nature of the accident scenario, limiting heat and hydrogen production as a result of zirconium oxidation at high temperatures and up to longer periods could effectively alter the outcome of the accident and reduce possibility of severe core degradation.

The current oxide fuel rods experience burst during a design basis LOCA owing to the rise in internal pressure at high temperatures. Rod burst results in steam ingress into the rod internals. In the case of M3 fuels, this is not a viable scenario since no pellet-cladding gap that could be pressurized exists. However, if protective iron alloy layers are to be considered for implementation into a composite cladding structure with conventional fuel, this issue needs to be taken into account. With steam on both sides of the cladding, a protective alloy layer would be needed on the outer and inner surfaces of the Zr alloy tube. Given that the interaction layer that forms between zirconium and the iron alloys studied here at high temperature is on the order of a few hundred micrometers thick, the total protective layer thickness (inner + outer) needed to protect the zirconium layer in the middle of the cladding will be roughly as thick as current LWRs cladding tubes (572 μm for 17 × 17 pressurized water reactor (PWR) bundles). Accordingly, composite iron alloy-zirconium cladding structures are deemed inferior to a single bulk Fe-base alloy cladding approach where the zirconium is eliminated altogether. While the two offer comparable neutronic penalties (higher neutron absorption in iron alloys compared to zirconium alloys), the latter is expected to perform better under high-temperature steam environments in the absence of detrimental Fe alloy–zirconium interactions.

The performance of specific Fe-base alloys under normal operating conditions in an irradiation environment has not yet been investigated and is beyond the limited scope of this study. Whether an Fe-based alloy is considered as a protective layer on the surface of M3 fuel rods or as cladding tubes, a comprehensive set of studies that examines materials and reactor physics aspects of these concepts needs to be performed. For instance, in the case of composite Fe-base alloy-zirconium structures, diffusion of alloy constituents into α-Zr under normal operating conditions after long periods needs to be considered [32]. Incorporation of thin Fe-alloy layer on the surface of the rod or cladding needs to be examined from a fabricability standpoint. Under irradiation, the evolution of dissimilar materials has the potential to prove problematic. Also, the presence of Fe-based alloy on the surface of Zr alloy can potentially result in hydrogen charging of the latter with significant impact on the mechanical properties.

4.2. Neutronic aspects of M3 fuels with an outer iron alloy layer

As previously reported [2], the limited heavy metal loading in M3 fuels, necessary due to the heterogeneous distribution of the fissile material, requires a transition to higher density fuel kernel materials as well as higher uranium enrichments. Incorporation of an Fe-base alloy layer at the rod surface brings about a larger neutronic penalty compared to the case where the entire rod is composed of zirconium. Single-pin reactivity calculations were performed to quantify the magnitude of reactivity loss upon incorporation of various outer Fe-base alloy layers. The TRITON module from the SCALE 6.1 package was utilized to perform these calculations [33]. Table 3 provides the configuration of various M3 rods

Table 3
Details of the M3 fuel pin configurations examined in Fig. 11.

	Case 1	Case 2	Case 3	Case 4
Kernel[a]	UN	UN	UN	UN
Packing fraction	0.42	0.42	0.42	0.42
Buffer thickness (μm)	70	70	70	70
Kernel diameter (μm)	750	750	750	750
IPyC, SiC (μm)[b]	35, 35	35, 35	35, 35	35, 35
Core diameter (mm)[c]	4.5	4.5	4.5	4.5
Outer layer thickness (μm)	200	400	400	400
Outer layer material	FeCrAl	FeCrAl	310SS	Zircaloy
Rod diameter (mm)	9.40	9.80	9.80	9.80
Pitch/diameter[d]	1.340	1.286	1.286	1.286

[a] Both UO$_2$ and UN densities are assumed at 96% TD (theoretical density).
[b] No OPyC layer is present in the coated fuel particles.
[c] Core is the area where Zircaloy metal matrix and particle mixture is located.
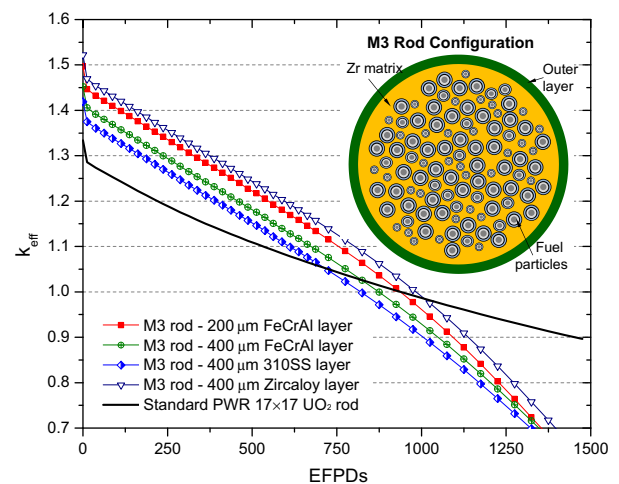[d] Constant pitch of 12.6 mm is assumed (based on reference 17 × 17 PWR bundle).

Fig. 11. Single-pin reactivity as a function of effective full power days for various M3 fuel pin configurations.

that have been examined through single pin burnup-dependent reactivity calculations in Fig. 11. The outer region of the rod that is free of any particles has been varied across various configurations. The results are plotted against the standard UO$_2$ rod in a 17 × 17 PWR bundle with 4.9% ^{235}U enrichment. Fig. 12 shows the reactivity penalty at the end-of-life (EOL) for various M3 fuel
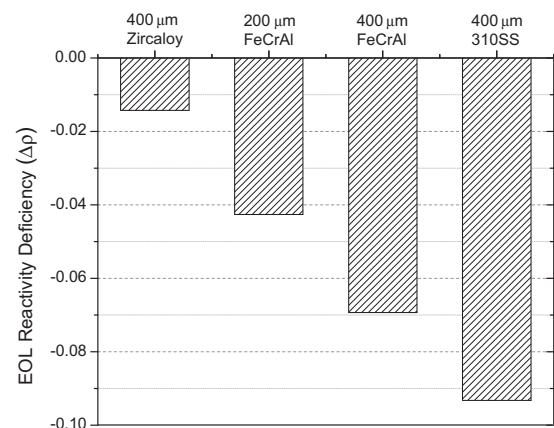

Fig. 12. Deviation of EOL core reactivity in M3 fuel rods with various outer layers from that of standard oxide fuel rod.

rod configurations against the standard UO_2 rod estimated with the linear reactivity model. The largest penalty is associated with an outer austenitic 310SS layer. This is expected since nickel possesses a large neutron absorption cross section.

5. Conclusions

Oxidation-resistant Fe alloy cans with $\sim$2 mm wall thickness effectively protected zirconium metal slugs from oxidation in high-temperature steam environments at 1200 °C and 1300 °C for up to 48 h. Ferritic, alumina-forming FeCrAl and austenitic chromia-forming Type 310 stainless steel were investigated based on their excellent oxidation resistance in steam under these conditions. Both alloy cans experienced significant interdiffusion with the zirconium metal that likely explains the failure of the 310SS can and oxidation of the Zr alloy slug after 8 h at 1300 °C. Interdiffusion resulted in a $\sim$200 μm thick intermetallic layer for the FeCrAl alloy. The intermetallic layer was twice as thick for the 310SS at 1200 °C. Based on the depth of interdiffusion and the current Zr alloy cladding thickness ($\sim$575 μm) utilization of a composite cladding structure, such as a Zr alloy placed between an inner and outer layer of Fe-base alloy, proves an inefficient solution from a neutronics perspective while providing marginal safety gains. A protective Fe-base alloy outer layer could provide a higher safety margins for M3 fuels under beyond design basis accidents; however, their utilization is also accompanied by a significant neutronic penalty.

Acknowledgements

References

[1] R.B. Adamson, Effects of neutron irradiation on microstructure and properties of Zircaloy, in: G.P. Sabol, G.D. Moan (Eds.), Zirconium in the Nuclear Industry: Twelfth International Symposium, ASTM STP 1354, American Society for Testing and Materials, West Conshohocken, PA, 2000, pp. 15–31.
[2] K.A. Terrani, L.L. Snead, J.C. Gehin, J. Nucl. Mater. 427 (2012) 209.
[3] K.A. Terrani, J.O. Kiggans, L.L. Snead, J. Nucl. Mater. 427 (2012) 79.
[4] L. Baker, L.C. Just, Studies of Metal–Water Reactions at High Temperatures, Argonne National Laboratory, Report ANL-6548, 1962.
[5] R.E. Pawel, J.V. Cathcart, J.J. Campbell, J. Nucl. Mater. 82 (1979) 129.
[6] M. Moalem, D.R. Olander, J. Nucl. Mater. 182 (1991) 170.
[7] Martin. Steinbrück, Nóra. Vér, Mirco. Große, Oxid. Met. 76 (2011) 215–232.
[8] J.P. Abriata, J. Garcés, R. Versaci, J. Phase Equlib. 7 (2) (1986) 116–124.
[9] T. Cheng, J.R. Keiser, M.P. Brady, K.A. Terrani, B.A. Pint, J. Nucl. Mater. 427 (2012) 396–400.
[10] K.A. Terrani, J.R. Keiser, M.P. Brady, T. Cheng, B.A. Pint, L.L. Snead, G.W.C. Silva, Transactions of TopFuel 2012, Manchester, United Kingdom, September 2012, (Paper A0128).
[11] B. A. Pint, M. P. Brady, J. R. Keiser, T. Cheng and K. A. Terrani, in: Proceedings of the 8th International Symposium on High Temperature Corrosion and Protection of Materials, Les Embiez, France, May 2012, (Paper#89)
[12] M. Jiang, K. Oikawa, T. Ikeshoji, L. Wulff, K. Ishida, J. Phase Equlib. 22 (4) (2001) 406–417.
[13] I. Ansara, COST 507: Thermochemical Database for Light Metal Alloys, European Commission, Directorate-General XII, Science, Research and Development, 1995.
[14] N. Wang, C. Li, Z. Du, F. Wang, CALPHAD 31 (4) (2007) 413–421.
[15] Raghavan V, Indian Inst. Met. 6B (1992) 711–721.
[16] H.I. Shaaban et al., J. Nucl. Mater. 71 (1978) 277–285.
[17] H.I. Shaaban, F.H. Hammad, J. Nucl. Mater. 78 (1978) 431–433.
[18] K. Bhanumurthy et al., J. Nucl. Mater. 185 (1991) 208–213.
[19] K.L. More, P.F. Tortorelli, M.K. Ferber, L.R. Walker, J.R. Keiser, W.D. Brentnall, N. Miralya, J.B. Price, J. Eng. Gas Turbines Power 122 (2) (2000) 212.
[20] M.M. Nowell, S.I. Wright, J. Microsc. 213 (Pt 3) (March 2004) 296–305.
[21] CM Parish et al., Microsc. Microanal. 17 (Suppl. 2) (2011).
[22] L. Kaufman, H. Bernstein, Computer Calculation of Phase Diagram, Academic Press Inc., New York, 1970.
[23] B. Sundman, B. Jansson, J.O. Andersson, CALPHAD 9 (2) (1985) 153–190.
[24] L. Shi, D.O. Northwood, Mater. 43 (2) (1995) 453460.
[25] S. Dryepondt, B.A. Pint, Mater. Sci. Eng. 497 (2008) 224.
[26] P. Hofmann, J. Nucl. Mater. 270 (1999) 194.
[27] M. Steinbrück et al., Nucl. Eng. Design 240 (2010) 1714.
[28] K. Kanematsu, Y. Fujita, J. Phys. Soc. Jpn. 29 (1970) 864.
[29] O. Canet et al., J. Alloys Compd. 210 (1994) 129–134.
[30] B.M. Pande et al., J. Nucl. Mater. 28 (1968) 324–332.
[31] F. Stein et al., J. Phase Equlib. 23 (6) (2002) 480.
[32] G.M. Hood, J. Nucl. Mater. 159 (1988) 149–175.
[33] M.D. DeHart, S.M. Bowman, Nucl. Technol. 174 (2) (2001) 196–213.